ORIGINAL ARTICLE

Mechanical properties, crystallographic texture, and in vitro bio-corrosion of low-alloyed Zn–Mg, produced by hot and cold drawing for biodegradable surgical wires

Andrij Milenin[1] · Mirosław Wróbel[1] · Piotr Kustra[1] · Marek Packo[1] · Dorota Byrska-Wójcik[1] ·
Joanna Sulej-Chojnacka[2] · Bartłomiej Płonka[3]

Abstract

The paper is devoted to the study of the mechanical, microstructural, and bio-corrosive behavior of low-alloyed Zn–Mg biodegradable surgical wires for bone reconstructions. Three biodegradable alloys with different magnesium content have been studied, their production technology has been developed and the product properties have been determined. The technology includes casting, extrusion, hot and cold drawing of the wire, and the product surface finishing. The paper shows the most important stages of the process (i.e., extrusion and drawing) in detail. The technological parameters have been selected based on the results of the computer modeling. The flow stress–strain curves of extruded materials have been obtained at various strain rates and temperatures. Two drawing technologies have been compared. The first one is the room temperature conventional wire drawing. In the second one, the first few passes have been made at an elevated temperature and the rest at room temperature. This allowed avoiding the breaking of the wire during the first passes (a typical issue of the conventional technology for these alloys) and increasing the ductility of the final product. Mechanical properties, bio-corrosion, and crystallographic texture of the material were determined at different stages of the processing. A simultaneous increase in the wire strength, the number of repeated bending until the rupture of the wire, and in the bio-corrosion rate due to drawing has been registered. This phenomenon coincided with a change in the crystallographic texture. It has been shown that the product tensile strength of about 250–300 MPa can be reduced by about 30% due to surgical knots tied on it.

Keywords Zn–Mg alloys · Sutures · Production · Corrosion · Relaxation · Texture

1 Introduction

The thermoplastic polymers are predominantly used in surgery as biodegradable materials. They are synthesized mainly from lactide or glycolide [1], and are known as the polylactic acid (PLA) and the polyglycolic acid (PGA) ones, respectively. Within 3–18 months [2], both of them have been degraded in a patient's body by hydrolytic or enzymatic processes forming water and non-soluble carboxyl-terminated oligomers, which are released into the environment. Despite that these polymers are treated as biocompatible ones, the adverse effects on the surrounding body can be observed due to their implantation [3]. The main problems are the local pH shifts and debris diffusion. Therefore, the swelling of the soft tissue can last up to 6 years after implantation [4]. Moreover, relatively low mechanical properties are an important disadvantage of the polymers. The Young's modulus of the PLA and PGA is in the range of 1.5–3.6 GPa and of 5–7 GPa, respectively [5]. The tensile strength is also relatively low {i.e., about 40–50 MPa for PGA and 15–75 MPa for PLA [6]}. The possibility of increasing the cross-sectional area is limited, because the volume of biodegradable material increases significantly and local injuries can be caused e.g. by ends of the surgical thread. For these reasons, monofilament surgical threads can only be used in

✉ Piotr Kustra
pkustra@agh.edu.pl

1   Faculty of Metals Engineering and Industrial Computer Science, AGH University of Science and Technology, al. Mickiewicza 30, 30-059 Kraków, Poland

2   Łukasiewicz Research Network-Metal Forming Institute, ul. Jana Pawła II 14, 61-139 Poznań, Poland

3   Division in Skawina, Łukasiewicz Research Network-Institute of Non-Ferrous Metals, ul. Piłsudskiego 19, 32-050 Skawina, Poland

smaller sizes [7]. On the other hand, multifilament surgical threads are more exposed to bacterial contamination and have a capillary effect which is also undesirable. Polymers also have a low creep resistance [8] what significantly limits the sterilization temperature and makes the sterilization process difficult. Therefore, a polymer cannot be recommended for high-strength biodegradable surgical applications. Broken bones, for example, are usually connected with a surgical stainless steel wire by pulling together parts of the bone and twisting the wire. In this case, a second operation is necessary for two reasons. The first is the removal of the wire, and the second is the timely unloading of the bone for a more effective healing [9].

A promising alternative for polymers and a stainless steel surgical wire could be surgical wires made from biodegradable metals and/or alloys, based on pure Fe, Mg, and Zn. Metals have a relatively high strength, in contrast to polymers used for the suture. The Young's modulus of magnesium is 45 GPa; hence, it is about ten times higher than for PGA. The Young's modulus of Zn is even higher and for Fe, it is very high. For pure zinc, it is equal to 94 GPa and 100–110 GPa for the Zn-based alloys. The Young's modulus of Fe alloys covers the range of 150–210 GPa. In contrast to polymers, the yield strength of the biodegradable metals is high {70–220 MPa, 150–296 MPa, and 170–1100 MPa for Mg alloys, Zn alloys, and Fe alloys, respectively [10]}; thus, there is no risk of a break or an uncontrolled plastic deformation, and its ductility is sufficient to make a surgical knot as it was shown elsewhere [8].

The sterilization of metal sutures is also much easier, because the creep resistance of Zn and Mg is sufficient and of Fe is exceeding the requirement. The biocompatibility of the considered metallic elements is also adequate because all of them (i.e., Fe, Mg, and Zn) are natural elements of the body and they take part in many processes in the organism.

Magnesium wires were successfully used for the first time as ligatures to stop bleeding vessels in a radial artery, and the operation for varicocele by E.C. Huse in 1878 [11] and in 1892 by E. Payr as biodegradable implants [12]. Some years later, magnesium was tested in vivo on rabbits and dogs by A. Lambotte [13]. These studies looked very promising. Indeed, magnesium has the highest recommended daily intake of 375–500 mg in human body [14] but, unfortunately, magnesium alloys have too high corrosion rates and insufficient ductility for this application [15]. Also, when magnesium corrodes, hydrogen is released. Together, these phenomena create a risk of local cytotoxicity [16].

One of the requirements for strong degradable materials is no more than a two-fold decrease in strength per 1 month of corrosion. It was shown in [15] that for Mg–Ca alloys, due to a too high rate of bio-corrosion, this condition is satisfied only for an extruded wire with a diameter of 1.8 mm, which is much larger than the diameter of steel wires usually used

for tightening bone tissues. There is also an important, up to 50%, decrease in the strength of the wire made of a magnesium alloy when a surgical knot is tied [8]. For these reasons, the first and subsequent studies on the use of magnesium and its alloys for producing surgical wires have not yet led to a widespread use of these materials in surgical practice.

The biodegradation of metallic Fe and Zn does not result in a gas release. Moreover, iron has sufficient mechanical properties. Unfortunately, the iron degradation rate in the mammalian body is too slow [17]. Another disadvantage is related to the iron ferromagnetism [18]. Therefore, the use of metallic iron in surgery is limited. Zinc has a fairly good biocompatibility in vivo, but the strength of metallic zinc is insufficient for many surgical applications [19]. An interesting feature of a zinc wire was noted in [20]. Unlike in magnesium alloys and polymers, the tensile strength of pure zinc is not sensitive to a surgical knot tied on the wire, (i.e., the tensile strength remains practically unchanged).

An overview of zinc's potential for use in biodegradable implants can be found in Ref. [21]. Fortunately, alloying can significantly strengthen zinc, e.g., the tensile strength of Zn–Mg alloys can easily reach about 350–400 MPa [22]. Some of such alloys have also a quite good biocompatibility determined during tests in vivo. Thus, after a 12 week test period, no inflammatory response in living tissue was reported by Kubásek et al. [22]. However, in vivo biocompatibility depends on the magnesium content in an alloy, as it was shown by Jin et al. [23]. Although pure magnesium has better biocompatibility than pure zinc, some increase in the magnesium content in Zn–Mg alloy worsens the alloy's biocompatibility in vivo. For this reason, zinc alloys with relatively small magnesium additions (up to wt. 0.1%) were proposed by Jin et al. [23] for some biomedical applications. The strength of such alloys can be sufficient for biomedical applications. The strength sensitivity to the strain rate of the alloys found by Jin et al. [23] was a phenomenon important not only for the wire operation but also for the design of the metal forming technology. However, no results of the plastometric properties of Zn–Mg alloys (i.e., the flow stress dependence on the strain, strain rate, and temperature) are available in the published papers. This significantly hampers the development of an effective technology for the production of such alloy wires. Thus, the determination of these properties was one of the objectives of the present work.

A relatively high stress relaxation property, much higher than in the case of steel and magnesium, is typical both for zinc and its alloys {e.g. see Milenin et al., 2019 [8]}. This phenomenon is often interpreted as a defect. However, it can be very useful in the surgical practice. In the initial and immediate process of bone reconnection, a high strength wire is required, but at some stage of the patient's recovery, the bones have fused together and they load carrying capacity increases; therefore, the load should be transferred to the

bones. The implant strength should be gradually reduced and finally the implant should dissolve completely. This may be a case for the zinc-based implants but their potential has not been sufficiently tested in the available literature. It is also worth taking a note of a complex dependence of the properties critical to the surgical applications not only on the chemical composition but also on the production technology, which in itself causes numerous problems. The processing route and the microstructure effect on the mechanical and bio-corrosive properties of the Zn–Mg alloys has been already reported by Liu et al. [24] and it can be related to the elasto-plastic anisotropy of zinc alloys typical for metals with the hexagonal-close packed (hcp) crystal structure. Verification of this hypothesis was another goal of this work.

The results of the tensile test are not sufficient to characterize the mechanical properties of the surgical wire. Thus, in this study, the standard tensile test has been supplemented by the tensile test of the wire with surgical knots tied on it and by wire bend tests. For Zn–Mg alloys, results of such studies have not been found in the available literature.

A significant part of the paper concerns the development of the plastic forming technology of Zn–Mg alloys. Such technologies have been proposed in the available literature. Galib and Sharif [25] manufactured different Zn–Mg alloys with the magnesium content in the range of 0.5–7.0 wt. % and found that the alloys with above 5 wt. % magnesium were so brittle that it was impossible to prepare tensile test specimens. Vojtěch et al. [26] reported that for Zn–Mg alloys with Mg content of 0–3% the elongation was less than 2%. The powder metallurgy route also does not allow obtaining Zn–Mg alloys with plasticity sufficient for practical application, as it was shown by Guleryuz et al. [27]. Saitz et al. [10] reported that up to the year 2015, surgical sutures would not be made from Zn–Mg alloys because of their insufficient plasticity. They said there would be a need to develop another class of Zn-based alloys. However, Okamura et al. [28] produced wires of 0.6 mm diameter from Zn–Mg alloy with Mg content in the range of 0.08–1.8% with the tensile elongation of about 10%. These wires were designed for some applications in urology. The production process was realized by a two-step extrusion from a diameter of 20–4.0 mm and then to the final diameter of 0.6 mm. Unfortunately, the bending and relaxation mechanical properties, which are important both for the manufacturing process and practical application, were not demonstrated in this work. In addition, the process developed by Okamura et al. seems too expensive for industrial implementation. The laboratory process combining extrusion and multi-pass cold drawing was present by us [29] but it was also not acceptable to the industry for the surgical treads production despite the bending test results being satisfactory. The technology of extrusion and subsequent hot drawing with annealing between passes was proposed by Seitz et al. [30] as a typical deformation

route in the manufacture of low melting point metal wires. However, this processing route is also not welcomed by the industry, because it does not provide many possibilities for controlling the properties and microstructure of the product. The technology proposed in paper [31] does not have this disadvantage. This technology, which is a combination of hot and cold drawing processes, was proposed and it was previously successively used by us for obtaining ultrafine wires (diameter 50 μm) from Mg–Ca alloys.

Thus, the paper is devoted to the study of the influence of hot and cold drawing on the mechanical properties (including specific ones), crystallographic texture, and bio-corrosion of wire made of Zn–Mg alloys, and the development on this basis of a production technology of biodegradable surgical wires based on Zn–Mg alloys. The technological parameters of the deformation processes were determined based on results of the finite element method (FEM) simulations using the flow stress–strain curves measured at various strain rates and temperatures and then verified and optimized during technological tests.

2 Materials and methods

2.1 Casting

The ingot material was produced by melting under a slag layer using a medium frequency induction industrial furnace. Technically, zinc (purity 99.995 wt. %Zn) was melted with magnesium (purity 99.92 wt. %Mg). The temperature should not significantly exceed the temperature optimum for the casting process. From the Zn–Mg phase equilibrium diagram, it follows that the point of liquidus falls with an increase in Mg content from about 420 °C for pure Zn to about 364 °C for $Zn–Mg_2Zn_{11}$ eutectic [32]. The chemical composition of the bath was controlled by a chemical analysis of samples taken periodically. The liquid alloy was poured into a round ingot mold with a diameter of 100 mm and length of about 320 mm. After complete cooling, the ingots were removed from the mold and cut with band scissors into 160 mm long sections. The ingot was mechanically machined to a diameter of 95 mm and then cut into two parts (with a length of 80 mm) used as the initial billet of extrusion. At the same time, the final sample for a chemical analysis was taken.

The chemical composition was determined by the atomic absorption spectrometry (AAS) method for the three casted variants: ZnMg0.0026 (0.0026 wt. %Mg + 0.005 wt. % total acceptable admixtures + Zn balance), ZnMg0.0068 (0.0068 wt. %Mg + 0.005 wt. % total acceptable admixtures + Zn balance), ZnMg0.08 (0.081 wt. %Mg + 0.005 wt. % total acceptable admixtures + Zn balance).

2.2 The FEM simulations

For FEM simulation of extrusion and drawing processes, the Qform software (www.qform3d.com) was used. An assumption of an incompressible material was applied during the simulation of the material plastic flow, just as it was done in Ref. [33]. For the calculations, tabular forms of the stress–strain curves determined during compression tests of the studied materials were used (see chapter 3.1). A couple of thermo-mechanical problems were solved. Both extrusion and drawing processes were modeled as non-stationary until a steady-state stage of the numerical solution was reached. The extrusion was modeled as a three-dimensional and wire drawing as a two-dimensional axisymmetric process.

Deforming tools (punch, die, and container) were modeled as solids. Since the alloys under consideration contained 99.992–99.9 wt% of Zn, the thermophysical properties of all alloys were taken as for pure Zn.

Friction conditions were simulated using the Qform database. For extrusion and drawing, a coefficient of friction of 1.0 (no lubricant) and 0.3 (mineral oil + graphite) was used, respectively. The FEM meshes were adapted according to the strain distribution. Bearing length of the extrusion die in the FEM simulation and in the experiment was 1.76 mm and was the same for all channels. All thermal boundary conditions were selected according to Qform database recommendation: for extrusion and drawing, the heat transfer coefficients upon the metal-die contact were 30,000 W/m^2 K and 3000 W/m^2 K, respectively. The lesser value was used for drawing with a lubricant. The coupled temperature problem for die and metal was considered (both for extrusion and drawing processes). Based on the heat transfer coefficient (150 W/m^2 K) from the furnace to the wire, the wire temperature was calculated.

2.3 Extrusion

The casted billet was extruded in a multi-channel die (Fig. 1a) on the wires with a diameter of 1.8 mm. The initial ingot temperature of 250 °C and the extrusion velocity of 0.5 mm/s were selected by an experimental correction of the parameters predicted by the FEM simulation. The FEM modeling showed that the effective strain of the material during extrusion reached tremendous values of 6.0–7.0 (Fig. 1b, c) and the deformation zone temperature was close to 284 °C (Fig. 1d, e). The symmetry of the deformation process (Fig. 1b) allowed to significantly speed up the calculations. The sample results of the calculation made for the alloy ZnMg0.0026 are shown in Fig. 1b–e. These results correspond to the position of the punch at mid-height of the ingot.
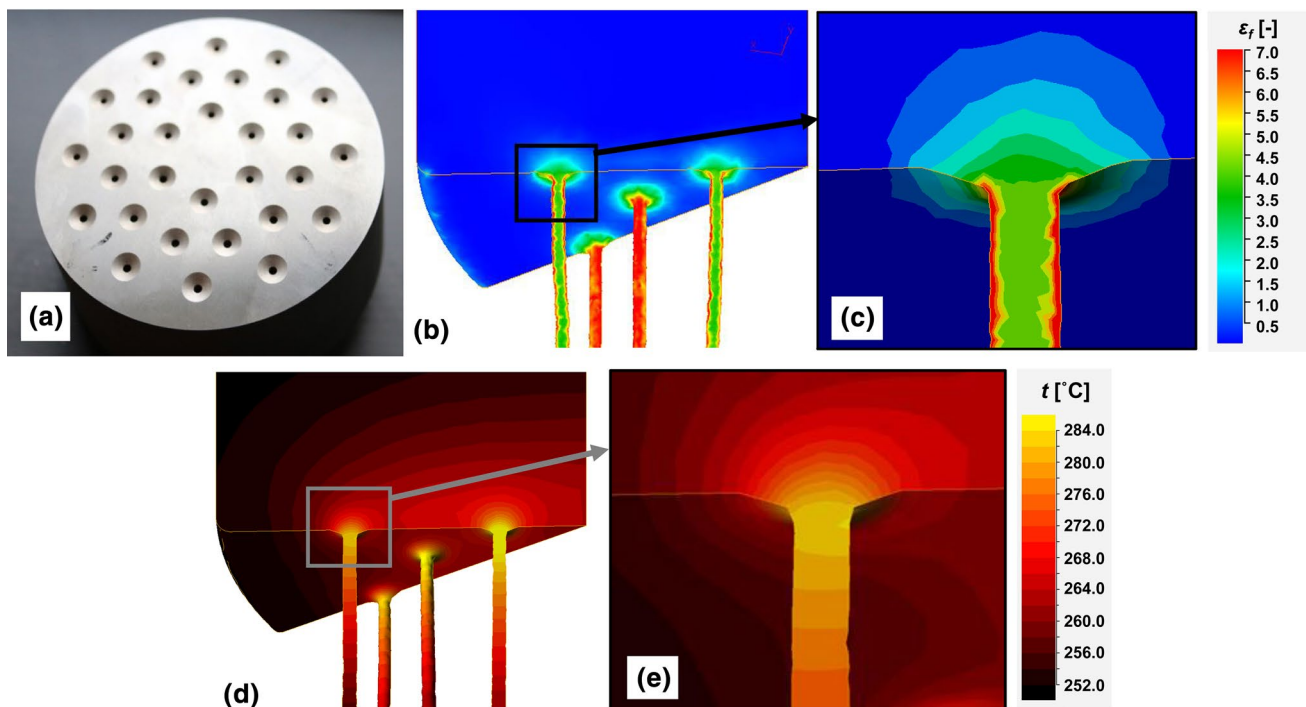

Fig. 1 FEM simulation of the extrusion process: (**a**) die for extrusion; the effective strain (**b**) and the temperature (**c**) distribution on the wire thickness calculated for the steady-state stage of extrusion. Figs. (**b**) and (**d**)—perspective, Figs. (**c**) and (**e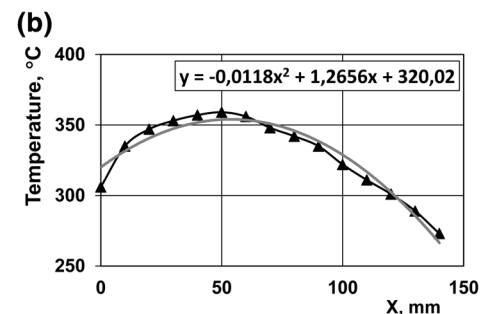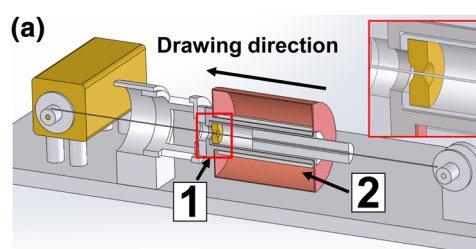**)—cross-sections. For different channels (holes in **a**), the differences in effective strain and temperature were insignificant (i.e. difference in the effective strain was negligible and in the temperature less than 10 °C)

2.4 Hot- and cold-drawing

The hot drawing schema is shown in Fig. 2a. Extruded rods with a diameter of 1.8 mm and a length of 2–5 m were unwound from a coil and heated during passing through a specially designed furnace (no. 2 in Fig. 2a) into a heated die (no. 1 in Fig. 2a). The die was mounted inside the furnace; therefore, the material was deformed at an increased temperature. After passing through the deformation zone, the wire was coiled with a precisely controlled speed and then cooled to room temperature. In such a process, the wire velocity affects not only the strain rate but also the deformation temperature. An increase in the drawing velocity decreases the heating time of the wire and lowers the deformation temperature. Therefore, the determination of the deformation temperature in such a process requires the FEM modeling. A similar drawing process was described by us in more detail elsewhere [31], where it was used for Mg–Ca alloy wires manufacturing. After the current pass had finished, the bobbins were swapped and the process was repeated. Diameters of the wire after the hot drawing passes were equal to (in mm): 1.8 (initial material); 1.724; 1.641; 1.561; 1.486; 1.414, and 1.346.

The furnace temperature distribution (Fig. 2b) was measured in separate experiments. In Fig. 2b, the drawing direction is from right to left, as in Fig. 2a; hence, the temperature for $X = 0$ mm corresponds to the die temperature. The drawing die's angle was 5°, the graphite base lubricant MOLYKOTE P-37 Thread Paste was used, and the drawing velocity was 10 mm/s. After the hot drawing, the wires were cleaned first with water with soap, then ultrasonically in ethanol, and finally dried out at room temperature. After this, the wires were drawn at room temperature according to schedule (in mm): 1.281; 1.219; 1.160; 1.104; 1.051; 1.00. In these cases, the liquid soap was used as a lubricant. Such a process will be referred to by us as a combined HT/RT drawing (HT—hot temperature, RT—room temperature). For comparison, the conventional wire drawing method was also used (i.e., the above passes were made at room temperature). However, in this case, surface cracks were observed on the wire coiled after the first pass, and from time to time the wire broke during winding.

2.5 Mechanical tests

The uniaxial compression tests of the extruded material were performed on a Zwick250 machine using small-size samples (diameter of 1.8 mm, height of 3 mm, Fig. 3a). A special die was manufactured for preparing such samples, in which 8 samples were simultaneously prepared (Fig. 3b). The die was printed from the ABS on a 3D printer and was used as a holder for the grinding process.

Compression final strain was equal to 0.8 and, during the test, the strain rate was of 0.01–2.0 s^{-1}. The resulting stress–strain curves were averaged from at least 2–3 tests. The mean square deviation of different curves from the mean did not exceed 6%. After the room temperature compression, stress relaxation was recorded for 60 s. The other tests were carried out at temperatures of 150 °C and 250 °C. In these experiments, the sample together with the deforming tools was heated to the test temperature; thus, heterogeneity in the sample temperature distribution was minimized. The lubricant based on graphite MOLYKOTE P-37 Thread Paste was used to reduce the friction of the deformed samples against the loading plates.

A standard tensile test of the final wire with a diameter of 1 mm was carried out at room temperature on a Zwick250 machine. During the tests, constant strain rates covering the range from 0.0035 to 0.071 s^{-1} were applied for simulation conditions arising when a surgical knot was being tied. The
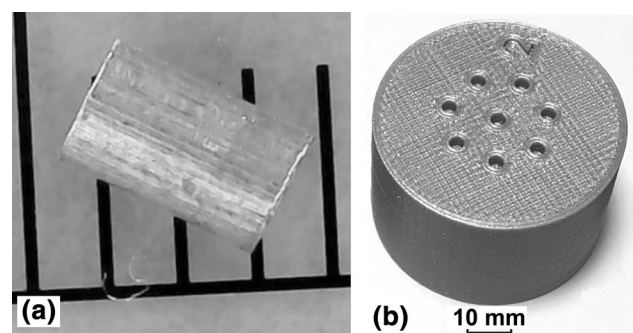
Fig. 3 Sample for uniaxial compressive tests (**a**) and the plastic tool used to prepare the samples (**b**)

Fig. 2 Scheme of the setup for the combined HT/RT drawing (**a**) and distribution of temperature from the heating device (**b**); 1—die; 2—heating device. Position of $X = 0$ mm in (**b**) corresponds to die 1 in (**a**)

$$y = -0.0118x^2 + 1.2656x + 320.02$$

length of the deformed part of the tested wire was equal to 200 mm. Conditions of the second tensile test were similar, but wires with surgical knots were used. The selected knots (see Fig. 4a, b) are usually applied in a bone surgery. Additionally, the ease of tying different surgical knots has been tested on plastic bone models (e.g., see Fig. 4c).

The reverse bend tests were carried out in the following standard—ISO 7801. The purpose of the test was to determine the wire ability to undergo plastic deformation during reverse bending and the number of bends before the wire breaks was recorded.

2.6 Biocorrosion

The 28 day in vitro corrosion tests were performed in a mixture of bovine serum supplied by Biowest (catalog No. S0250). Protein content in the mixture was equal to 30 g/l. Sodium azide (0.3 wt.%) and 20 mM of the ethylenediaminetetraacetic acid were added to the solution to inhibit bacteria growth and to bind calcium ions. The mixture was filtered through a sterile filter (pore size 20 μm). During the corrosion tests, the pH value and the temperature of the corrosion medium were kept equal to 7.2–7.4 and 37 ± 0.1 °C, respectively. The protein concentration was monitored by a GenesysTM20 spectrophotometer (Spectronic Instruments, USA). On day 3, 7, 14, 21, and 28, the samples were removed from the corrosion medium and a change in their weight was determined using a laboratory balance with an accuracy of 0.00001 g. Immediately before the test and before each weighing, the samples were thoroughly cleaned first in the distilled water and then ultrasonically in ethanol, and finally dried out at room temperature. During the in vitro

corrosion test, all recommendations provided by the ASTM F732-00 standard have been met.

2.7 The surface characterization and XRD study

Zinc is usually covered by a surface film which can significantly influence corrosion. Therefore, from the bio-corrosion point of view, the surface and subsurface layers of the material may be relevant. Therefore, X-ray diffraction (XRD) from such layers was measured. Thus, the cylindrical surface of the wire (i.e., parallel to the extrusion/drawing direction) was exposed to the Cu-Kα radiation. The Empyrean diffractometer by PANalytical was used. The data were collected during the continuous scan carried out in the reflective mode applying parallel beam geometry (Göbel mirror in the incident beam optics and parallel plate collimator in the diffracted beam). The orientation distribution function (ODF) and complete pole figures were calculated from the incomplete pole figures with the LaboTex software (http://www.labosoft.com.pl). The classical Williamson-Hall method was used for the crystallite size measurement [34].

3 Results and discussion

3.1 Extruded materials

The results of the room temperature compression in the extrusion direction are shown in Fig. 5. Some strong dependence of the flow stress on the strain rate can be seen. All curve maxima shift to a higher strain with an increase in the strain rate. On average, positions of the curve maxima correspond to the strain of 0.05–0.15. This means that even

Fig. 4 Surgical knots selected for this paper: a—the first type of a surgical knot used to tighten the tissue after a fracture; b—the second type of a surgical knot (i.e., the marine knot); c—the bone surgery simulation
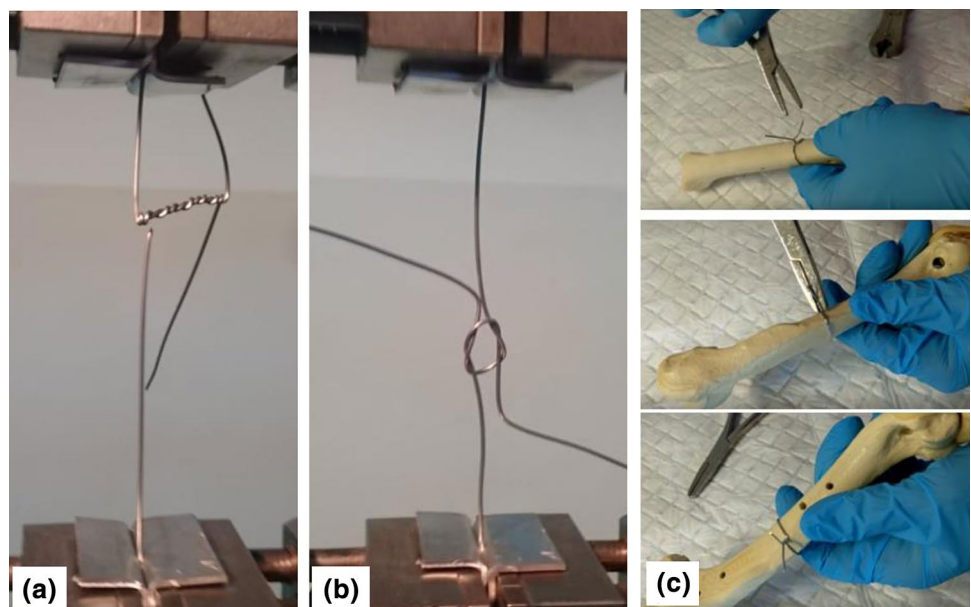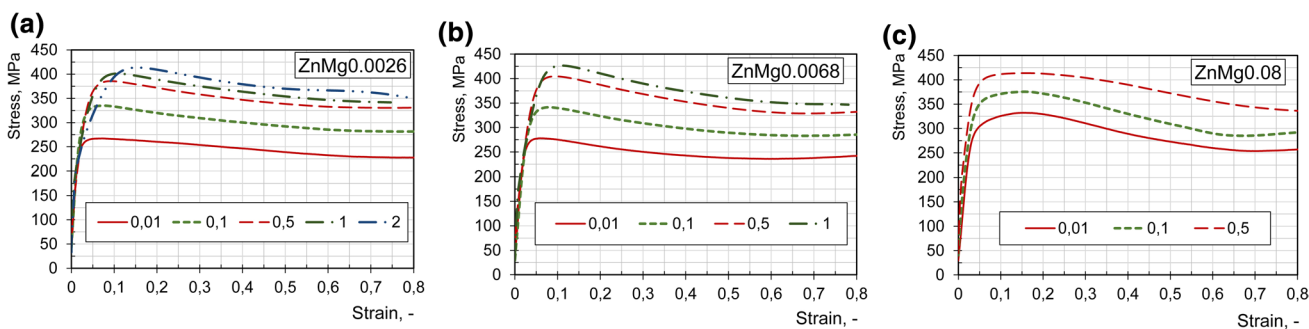
Fig. 5 Results of the plastometric tests of extruded material at room temperature for strain rates 0.01 s-1, 0.1 s-1, 0.5 s-1, 1 s-1 and 2 s-1: **a**—ZnMg0.0026; **b**—ZnMg0.0068; **c**—ZnMg0.08
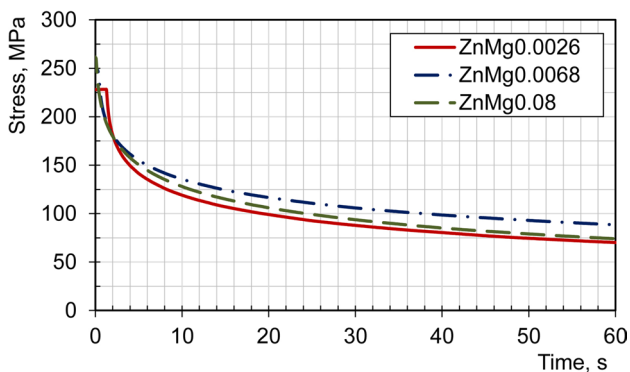

Fig. 6 Uniaxial compression stress relaxation of extruded material at room temperature after deformation with strain rate 0.01 s-1

during cold drawing with a low speed, some dynamic recrystallization can take place in the material.

The stress relaxation phenomenon was observed for all samples tested at room temperature. An illustrative result obtained for the strain rate of 0.01 s^{-1} is shown in Fig. 6. The results for other strain rates differ slightly. In Fig. 6, we can see more than a two-time decrease in the compressive stress value during 60 s of the relaxation. Such a rate of relaxation

is far too fast for practical purposes and a special technique for tying knots is required. An effect of the relaxation on healing requires additional studies.

Some typical results of the compression tests carried out at temperatures of 150–250 °C are shown in Fig. 7. The flow stress reduction in comparison to results of the room temperature tests is evident. However, the shape of the curves determined at different temperatures is a bit similar, as are the locations of their maxima and their shift towards higher strains due to an increase in the strain rate. A significant increase in the flow stress at a strain greater than 0.4, registered for all three alloys but only for the deformation temperature equal to 150 °C and a strain rate of 0.5 s^{-1}, can be related to the temperature characteristic of the friction between the samples and loading plates. Alternatively, this effect can be explained using the theory of rheologically complex materials developed by Shlomchak et al. in [35, 36]. A deeper analysis of this effect requires additional studies. Fortunately, the deformation developed at each drawing pass did not exceed 0.2; hence, this phenomenon is insignificant for this work.

The extruded rods are characterized by a texture with {002} crystallographic planes (i.e., the planes perpendicular to the c axis of the crystal lattice cell) in the position
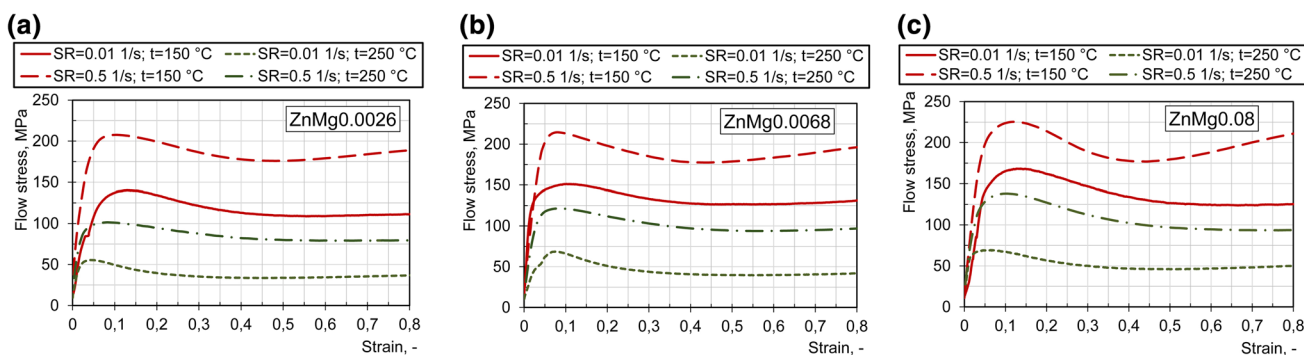

Fig. 7 Results of the plastometric tests of extruded material in temperatures 150 °C and 250 °C for strain rates 0.01 s-1 and 0.5 s-1: **a**—ZnMg0.0026; **b**—ZnMg0.0068; **c**—ZnMg0.08

parallel to the wire axis (Fig. 8). Such a texture can be formed during hot extrusion of the metals with an hcp structure and the ratio of the lattice cell parameters c/a greater than the one for the ideal hcp structure (which is energetically unstable [37] and for which the value is equal to 1.633). For zinc, this ratio is equal to 1.856. Some differences in the texture of the alloys with different alloying can be seen, but some single orientations were marked for all investigated alloys with can be related to relatively large grains. A large grain can be developed in the hot-deformed metals with a low melting point temperature, such as zinc for which the extrusion was carried out at the homologous temperature of 0.76.

3.2 FEM simulation of cold and hot drawing

For this paper, exemplary results obtained for the first pass of cold and hot drawing have been selected (Fig. 9a, b and Fig. 9c, d, respectively). All process conditions except the temperature were the same (i.e., one material was deformed at room temperature, the other in an increased temperature zone with the temperature profile shown in Fig. 2b). For hot drawing, the metal temperature in the deformation zone was about 200 °C (Fig. 9c). During cold drawing, the temperature of the material in the deformation zone was 37 °C (Fig. 9a). The strain distribution during cold and hot drawing differed insignificantly (maximal effective strain was 0.184 for cold drawing and 0.182 for hot drawing).
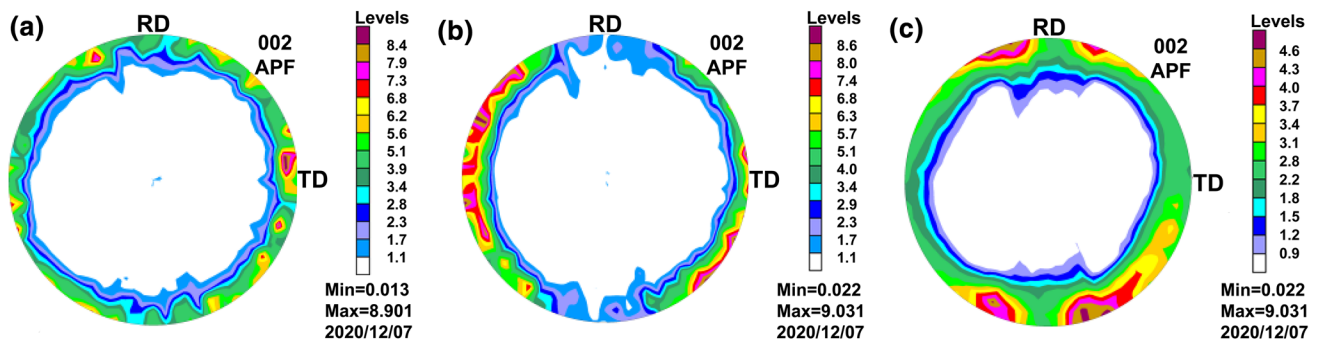

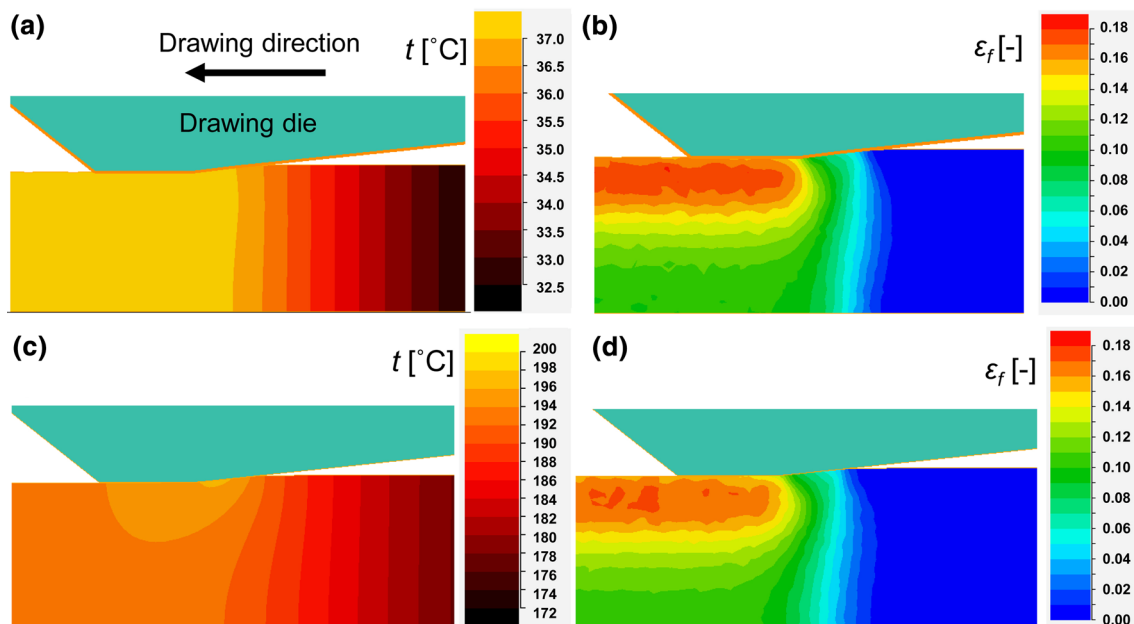**Fig. 8** Textures of extruded rods: **a**—ZnMg0.0026; **b**—ZnMg0.0068; **c**—ZnMg0.08

Fig. 9 FEM simulation of the cold (**a, b**) and hot (**c, d**) drawing process: **a, c**—distribution of the temperature; **b, d**—distribution of the effective strain

Fig. 10 Results of the UTS measurement at strain rate 0.005 s-1 after different stages of processing: $d = 1.77$ mm— after extrusion; $d = 1.34$ mm— after the first 5 passes of cold (**a**) and hot (**b**) drawing; $d = 1.0$ mm—after the last passes of cold drawing
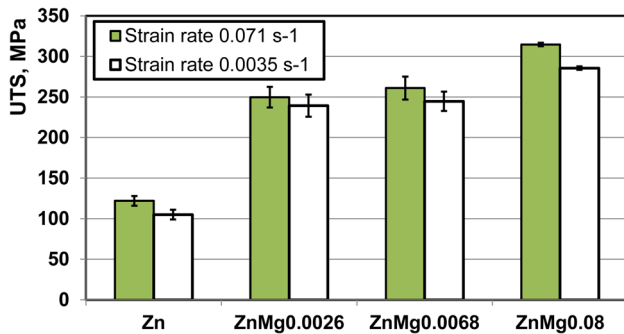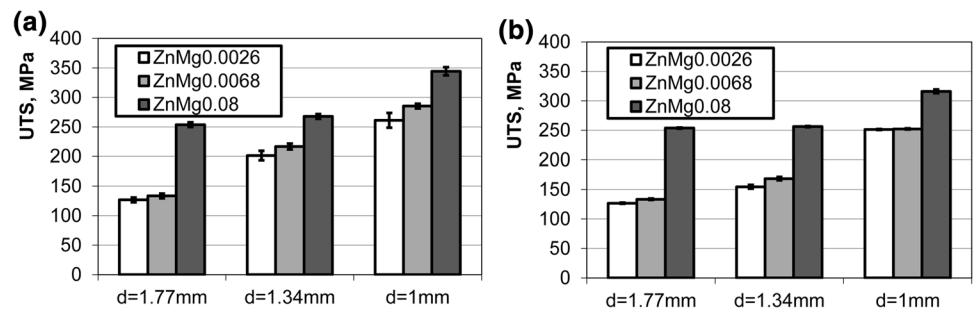

Fig. 11 Results of the UTS measurement of the final wire $d = 1.0$ mm for different materials and strain rates

Table 1 The knot weakening factor of the wire with a diameter equal to 1.0 mm

Material	Pure Zn	ZnMg0.0026	ZnMg0.0068	ZnMg0.08
Knot in Fig. 4a (type 1)	0.93	0.67	0.72	0.71
Knot in Fig. 4b (type 2)	0.97	0.75	0.77	0.76

In the cross-section of the wire, the distribution of strain is uneven. On the surface, the effective strain is about 0.19, but in the area of the wire axis, it is close to 0.11. The strain rate differs accordingly. In our case, the difference between the effective strain of the surface and the center of the wire is important from the point of view of bio-corrosion, since the surface volumes of the wire corrode first.

3.3 Drawn materials

Sample results of the tensile test of the final wire with a diameter of 1.0 mm, manufactured using conventional and combined HT/RT drawing, are collected in Fig. 10. The data were obtained at a tensile strain rate of 0.005 s^{-1} (for a wire 200 mm long this corresponded to a tensile rate of 1 mm s^{-1}). Some reduction in material strength after the first passes of the hot drawing compared to the one from RT drawing was evident and this could be related to recrystallization. However, an about 100 MPa increase in relation to the extruded material was recorded regardless of the drawing temperature tested. The achieved values are close to the strength of the wire made of magnesium alloys by Seitz et al. [30] and by Milenin et al. [31] and are sufficient for the practical use of the obtained material as a surgical wire.

The effect of the strain rate on the strength was shown only for the wire obtained by the combined HT/RT drawing (Fig. 11). A several percent increase in strength as a result of

a 20-fold increase in the strain rate can be seen. However, it is not significant from a practical point of view. A more than two-time greater strength of the final alloying wire than its pure zinc counterpart is of a significant practical importance.

An effect of a surgical knot on the strength was also presented only for the wire obtained by the combined HT/RT drawing and for the tensile rate equal to 8.3 mm/s. In this case, the strain rate was difficult to determine due to the complex configuration of the knots. The ratio of tensile strength of the knotted wire to its counterpart without knots will be called the knot weakening factor (KWF). The results are collected in Table 1 and presented in Fig. 4a, b. The results revealed that the KWF value of zinc is 20-something percent higher than that for low-alloyed Zn–Mg, which in turn does not depend on the magnesium content. The standard deviation of the results in Table 1 does not exceed 16%. A similar effect was previously reported by us [20]. The novelty of the paper is showing that the KWF value significantly depends on the type of the knot. It is worth noting that for all the cases listed in Table 1, the KWF value is significantly higher than for magnesium and surgical polymers MonosynR 2-0 and PolysorbTM 3-0, for which it is equal to 0.5, 0.61, and 0.47, respectively [8].

The tensile elongation (A_{200}) results collected in Table 2 show that the extruded material ductility is very close to that for the one drawn. However, this parameter is not a good enough indicator of a wire ductility. Susceptibility to multiple reverse bending is a much better parameter. Some results of the reverse bending test were collected in Fig. 12. We can see that the breakage of the wire with a diameter of 1.0 mm manufactured by combined HT/RT and the one conventionally drawn requires about 60 and 40 bends, respectively. On the other hand, extruded materials cannot

Table 2 A_{200} elongation (%) of wires at different stages of drawing

Material	ZnMg0.0026	ZnMg0.0068	ZnMg0.08
Extruded, $d=1.8$ mm	4.54 ± 0.04	4.80 ± 0.37	12.89 ± 0.14
After hot drawing, $d=1.34$ mm	7.62 ± 1.80	8.45 ± 0.82	9.82 ± 0.42
After cold drawing, $d=1.0$ mm	5.97 ± 0.87	9.87 ± 1.27	7.31 ± 0.05

withstand even one bend. This is one of the reasons for the fracture of the material during cold drawing especially during the first passes. Fortunately, the bends number increases sharply after a total elongation of 0.3–0.5.

A decrease in the sample mass in function of the time during in vitro corrosion is shown in Fig. 13. No apparent continuous effect of the magnesium content can be seen. On the other hand, the figure clearly shows an effect of the deformation. Thus, a decrease in the mass significantly increased with the deformation imposed during drawing (i.e., with a reduction in the wire diameter). This effect is shown more clearly in Fig. 14, where the dependence of the corrosion rate on the corrosion time is shown. The corrosion rate (CR), expressed in mm/year, has been calculated from the formula:

$$CR = 365 \frac{m_0 - m_{corr}}{\rho A \tau},$$

where m is the mass (in grams) of the sample before (m_0) and after (m_{corr}) corrosion for a given time τ (in days).
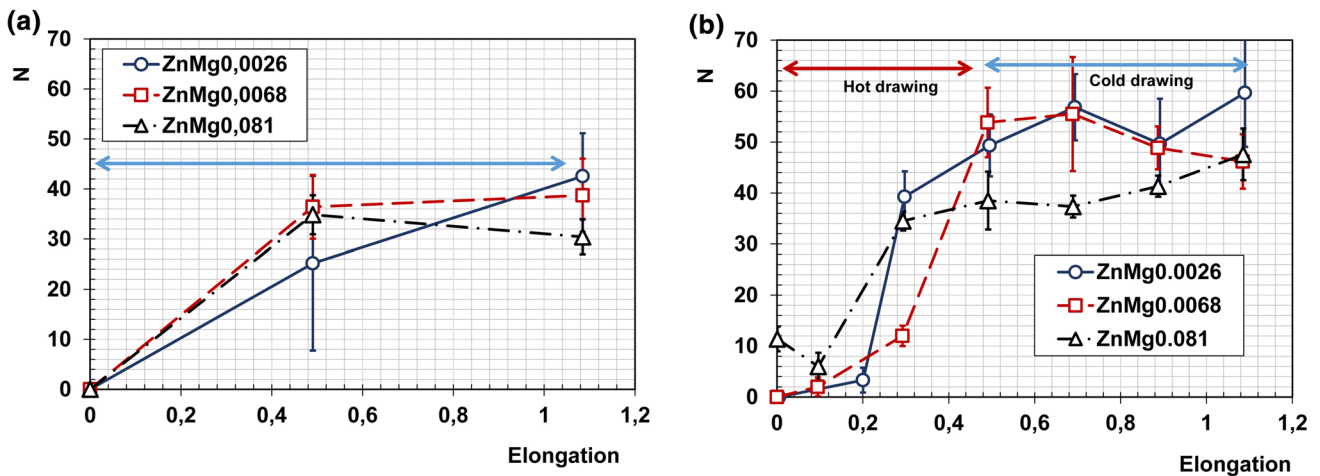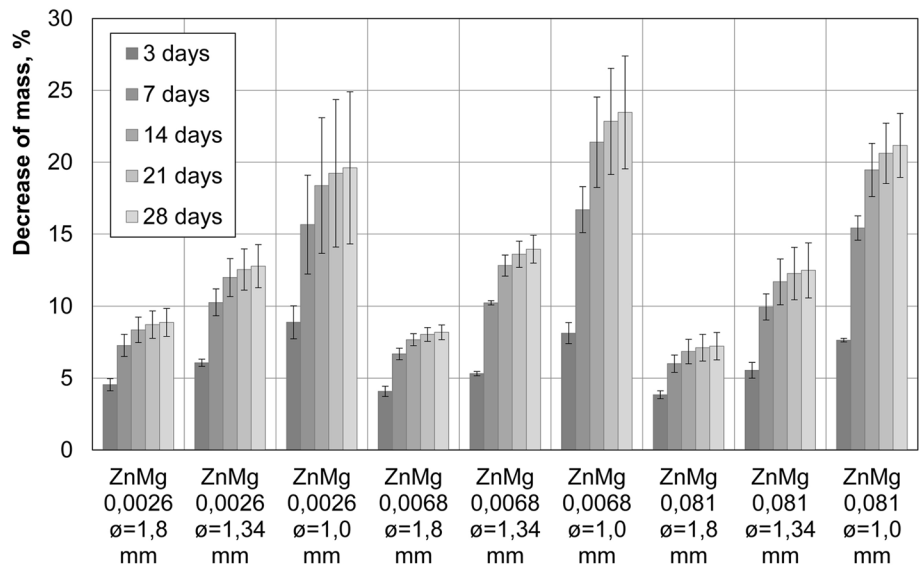

Fig. 12 Results of the measurement of the double bending test of a wire at different stages of drawing: **a**—cold drawing; **b**—HT/RT drawing

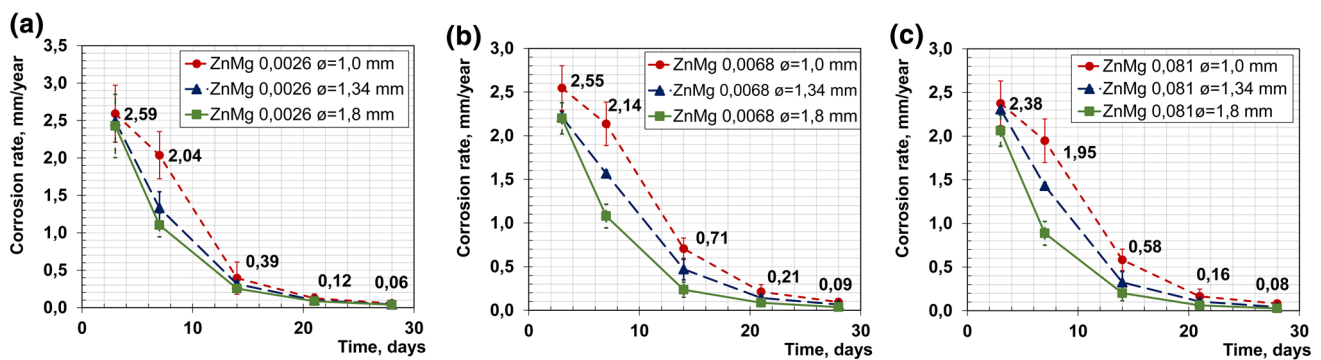**Fig. 13** Decrease of the mass of the samples during biocorrosion

Fig. 14 Corrosion rate measured after: extrusion ($d=1.8$ mm), first 5 passes of hot drawing to $d=1.34$ mm, and final cold drawing to $d=1.0$ mm; **a**—ZnMg0.0026, **b**—ZnMg0.0068, **c**—ZnMg0.08

A is the sample surface exposed to corrosion at each stage of the corrosion test (in mm^2), and ρ is the alloy density (in this study assumed to be equal to 7.14×10^{-3} g/mm^3). The calculations were carried out for adjacent time intervals; therefore, the obtained values represent the average corrosion rate at time intervals of 1–3, 3–7, 7–14, 14–21, and 21–28 days. Some decrease in the corrosion rate over time is clearly visible in Fig. 14. This figure also shows that the deformation effect is clearly visible in the first 20 days of corrosion. This may be related to some heterogeneity in the strain distribution along the wire thickness, predicted by the FEM simulations (see Fig. 9). Over time, the outer layers of the material with a greater deformation dissolve relatively fast in the corrosive mixture. The deformation in the middle layers of the wires is much lower; hence, the corrosion rate decreases. Based on data shown in Fig. 14, we can attempt to see a combined effect of the chemical composition and deformation on the corrosion rate and then to connect it with a difference in the subsurface layers' structure. However, this requires detailed research beyond the scope of this work and we consider the formulation of such conclusions to be far too premature.

The corrosion rates on the 28th day determined by us correlate well with the data published by Jin et al. [23] for in vivo corrosion of alloys with a similar chemical composition. Based on the data shown in Fig. 15, it is possible to predict the rate of complete dissolution of the wire. Assuming 20–25% weight loss during the first month and further corrosion rate as equal to 0.12–0.18 mm in a wire diameter per year, we can predict that a wire with an initial diameter of 1 mm will completely dissolve in the body after about 4 years. For a wire with a diameter of 0.8 mm, this would require about 3 years. These times are definitely too long. However, the above approximations are very rough and require verification.

No significant difference in the microstructure was found. The differences in the size of the crystallites were within the range of the measurement error (Table 3). Therefore, the reasons for the difference in the properties (number of double bending in Fig. 12) can be sought in some differences in the crystallographic texture. The textures of the drawn materials are shown in Fig. 15. A comparison with Fig. 8 shows that hot drawing causes the texture rotation and the {002} planes become inclined or nearly perpendicular to the axis of the wire (Fig. 15a, b, c). For the hot drawing wire with a diameter of 1.34 mm, the sharpest texture was developed in the ZnMg0.0068 alloy. For the texture, {002} planes were perpendicular to the wire axis. A similar type of texture was developed in ZnMg0.0024 but, in this case, the orientation spread was higher. Texture of the wire made from ZnMg0.08 can be characterized by the {002} planes both in the perpendicular and inclined position to the wire axis and some amount of the extruded material texture can also be seen.

Similar textures but without the extrusion texture component and with different relative shares of other two components were developed during the room temperature drawing (Fig. 15d, e, f). The observed clear differences in the texture of the extruded and the drawn materials can cause differences in their corrosion and mechanical properties (i.e., in the number of bends required for the wire to break). The corrosion rate depends on the surface atom density; hence, some relation of the corrosion rate to the crystallographic texture can be expected. High plastic anisotropy is typical for hcp metals; thus, the dependence of ductility on the crystallographic texture is also not surprising.

4 Conclusions

A technology for the manufacture of wires from ZnMg0.0026, ZnMg0.0068, and ZnMg0.08 alloys was proposed. The technology includes melting, casting, extrusion, and hot and cold drawing. Plastic working parameters were selected based on the results of computer modeling using the finite element method combined with the result of the
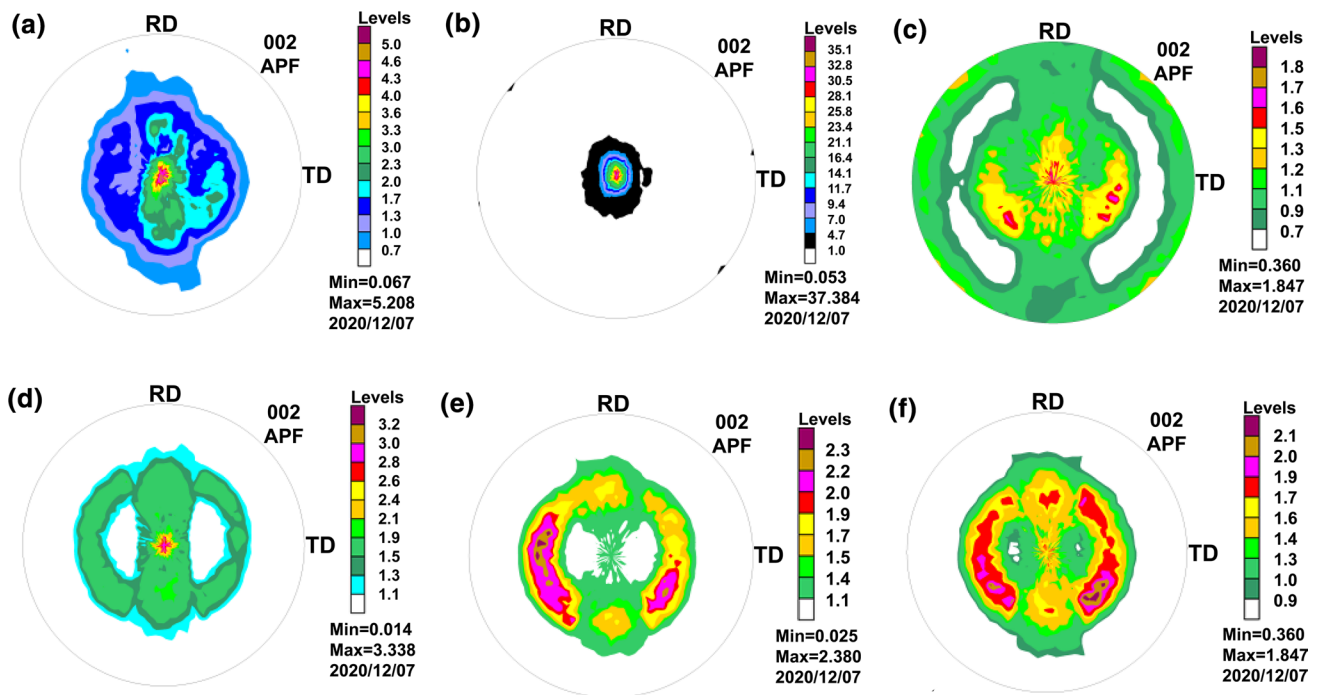
Fig. 15 Results of texture investigation for the wire after hot drawing to a diameter of 1.34 mm (**a**, **b**, **c**) and subsequent cold drawing to a diameter of 1.0 mm (**d**, **e**, **f**) for materials ZnMg0.0026 (**a**, **d**), ZnMg0.0068 (**b**, **e**), ZnMg0.08 (**c**, **f**)

Table 3 The crystallite size in A

	Crystallite size, A		
	ZnMg0.0026	ZnMg0.0068	ZnMg0.08
Extruded, $d = 1.8$ mm	378 (58)	327 (21)	323 (26)
After hot drawing, $d = 1.34$ mm	348 (42)	320 (37)	330 (26)
After cold drawing, $d = 1.0$ mm	338 (21)	286 (33)	338 (21)

technological tests. The essential properties of the product and its intermediates have been determined. The most important conclusions are summarized below.

1. The proposed technology allows obtaining a product of good quality. The use of a process combining initial drawing at an elevated temperature and subsequent drawing at room temperature allows completely avoiding the generation of wire cracks. The cracks cause breakage of the wire in the first passes of the classic drawing technology.

2. The ductility of the extruded semi-product, determined in the multiple bending test, is far too insufficient for its practical applications. However, it can be greatly improved during drawing. This change is caused by a change in the crystallographic texture that determines plastic anisotropy.

3. The product strength and ductility exceed requirements of the biomedical applications. However, the rate of biocorrosion, determined by in vitro tests in a mixture that imitates body fluids, is far too small for its use in bone surgery as bioabsorbable implants.

4. The presence of surgical knots reduces the strength of the material to an extent depending on the type of the knot. In the case of the tested materials, this reduction is much smaller than for typical polymers used for surgical sutures. However, standard testing of the effect of various knots used in surgical practice on the wire's strength is recommended.

5. The rate of in vitro bio-corrosion in a mixture imitating body fluids increases with the deformation induced during both the hot and the room temperature working.

Declarations

Conflict of interest The authors have no relevant financial or non-financial interests to disclose. The authors have no conflicts of interest to declare that are relevant to the content of this article. All authors certify that they have no affiliations with or involvement in any organization or entity with any financial interest or non-financial interest in the subject matter or materials discussed in this manuscript. The authors have no financial or proprietary interests in any material discussed in this article.

Ethical approval This paper does not contain any studies with human participants or animals performed by any of the authors.

References

1. Barrows T. Degradable implant materials: a review of synthetic absorbable polymers and their applications. Clin Mater. 1986;1:233–57. https://doi.org/10.1016/S0267-6605(86)80015-4.
2. Middleton JC, Tipton AJ. Synthetic biodegradable polymers as orthopedic devices. Biomaterials. 2000;21:2335–46. https://doi.org/10.1016/S0142-9612(00)00101-0.
3. Böstman O, Pihlajamäki H. Clinical biocompatibility of biodegradable orthopaedic implants for internal fixation: a review. Biomaterials. 2000;21:2615–21. https://doi.org/10.1016/S0142-9612(00)00129-0.
4. Bergsma EJ, Rozema FR, Bos RR, de Bruijn WC. Foreign body reactions to resorbable poly(L-lactide) bone plates and screws used for the fixation of unstable zygomatic fractures. J Oral Maxillofac Surg Off J Am Assoc Oral Maxillofac Surg. 1993;51:666–70. https://doi.org/10.1016/s0278-2391(10)80267-8.
5. Daniels AU, Chang MK, Andriano KP. Mechanical properties of biodegradable polymers and composites proposed for internal fixation of bone. J Appl Biomater. 1990;1:57–78. https://doi.org/10.1002/jab.770010109.
6. Marques DR, dos Santos LA, Schopf LF, de Fraga JCS. Analysis of poly(lactic-co-glycolic acid)/poly(isoprene) polymeric blend for application as biomaterial. Polímeros. 2013;23:579–584. http://www.scielo.br/scielo.php?script=sci_arttext&pid=S0104-14282013000500002&nrm=iso. Accessed 8 Mar 2021
7. Meyle J. Suture materials and suture techniques. Perio. 2006;3:253–68.
8. Milenin A, Kustra P, Wróbel M, Paćko M, Byrska-Wójcik D. Comparison of the stress relaxation of biodegradable surgical threads made of Mg and Zn alloys and some commercial synthetic materials. Arch Metall Mater. 2019. https://doi.org/10.2442/amm.2019.129506.
9. Bergsma JE, de Bruijn WC, Rozema FR, Bos RRM, Boering G. Late degradation tissue response to poly(L-lactide) bone plates and screws. Biomaterials. 1995;16:25–31. https://doi.org/10.1016/0142-9612(95)91092-D.
10. Seitz J-M, Durisin M, Goldman J, Drelich JW. Recent advances in biodegradable metals for medical sutures: a critical review. Adv Healthc Mater. 2015;4:1915–36. https://doi.org/10.1002/adhm.201500189.
11. Huse EC. A new ligature? Chicago Med J Exam. 1878;37:171–2.
12. Witte F, Hort N, Vogt C, Cohen S, Kainer KU, Willumeit R, Feyerabend F. Degradable biomaterials based on magnesium corrosion. Curr Opin Solid State Mater Sci. 2008;12:63–72. https://doi.org/10.1016/j.cossms.2009.04.001.
13. Lambotte A. Technique et indications de prothèse perdue dans la traitement des fractures. Press Med Belge. 1909;17:321–3.
14. Seitz J-M, Eifler R, Bach F-W, Maier HJ. Magnesium degradation products: effects on tissue and human metabolism. J Biomed Mater Res A. 2014;102:3744–53. https://doi.org/10.1002/jbm.a.35023.
15. Milenin A, Kustra P, Byrska-Wójcik D, Wróbel M, Paćko M, Sulej-Chojnacka J, Matuszyńska S, Płonka B. The effect of in vitro corrosion on the mechanical properties of metallic high strength biodegradable surgical threads. Arch Civ Mech Eng. 2020;20:60. https://doi.org/10.1007/s43452-020-00062-w.
16. Fischer J, Pröfrock D, Hort N, Willumeit R, Feyerabend F. Improved cytotoxicity testing of magnesium materials. Mater Sci Eng B Solid-State Mater Adv Technol. 2011;176:830–4. https://doi.org/10.1016/j.mseb.2011.04.008.
17. Schümann K, Ettle T, Szegner B, Elsenhans B, Solomons NW. On risks and benefits of iron supplementation recommendations for iron intake revisited. J Trace Elem Med Biol. 2007;21:147–68. https://doi.org/10.1016/j.jtemb.2007.06.002.
18. Wegener B, Sievers B, Utzschneider S, Müller P, Jansson V, Rößler S, Nies B, Stephani G, Kieback B, Quadbeck P. Microstructure, cytotoxicity and corrosion of powder-metallurgical iron alloys for biodegradable bone replacement materials. Mater Sci Eng B Solid-State Mater Adv Technol. 2011. https://doi.org/10.1016/j.mseb.2011.04.017.
19. Venezuela JJD, Johnston S, Dargusch MS. The prospects for biodegradable zinc in wound closure applications. Adv Healthc Mater. 2019;8:e1900408. https://doi.org/10.1002/adhm.201900408.
20. Milenin A, Kustra P, Byrska-Wójcik D, Wróbel M, Packo M, Sulej-Chojnacka J, Matuszynska S. Production of zinc wire for use as a high strength biodegradable surgical threads. Procedia Manuf. 2020. https://doi.org/10.1016/j.promfg.2020.08.136.
21. Levy GK, Goldman J, Aghion E. The prospects of zinc as a structural material for biodegradable implants—a review paper. Metals (Basel). 2017. https://doi.org/10.3390/met7100402.
22. Kubásek J, Dvorský D, Šedý J, Msallamová Š, Levorová J, Foltán R, Vojtěch D. The fundamental comparison of Zn–2Mg and Mg–4Y–3RE alloys as a perspective biodegradable materials. Materials (Basel). 2019. https://doi.org/10.3390/ma12223745.
23. Jin H, Zhao S, Guillory R, Bowen PK, Yin Z, Griebel A, Schaffer J, Earley EJ, Goldman J, Drelich JW. Novel high-strength low-alloys Zn–Mg (< 0.1 wt% Mg) and their arterial biodegradation. Mater Sci Eng. 2018;84:67–79. https://doi.org/10.1016/j.msec.2017.11.021.
24. Liu S, Kent D, Doan N, Dargusch M, Wang G. Effects of deformation twinning on the mechanical properties of biodegradable Zn–Mg alloys. Bioact Mater. 2019;4:8–16. https://doi.org/10.1016/j.bioactmat.2018.11.001.
25. Galib RH, Sharif A. Development of Zn–Mg alloys as a degradable biomaterial. C Int Publ Adv Alloy Compd. 2016. https://doi.org/10.7726/aac.2016.1001.

26. Vojtěch D, Kubásek J, Serák J, Novák P. Mechanical and corrosion properties of newly developed biodegradable Zn-based alloys for bone fixation. Acta Biomater. 2011;7:3515–22. https://doi.org/10.1016/j.actbio.2011.05.008.

27. Guleryuz LF, Ipek R, Arıtman I, Karaoglu S. Microstructure and mechanical properties of Zn–Mg alloys as implant materials manufactured by powder metallurgy method. AIP Conf Proc. 2017;1809:20020. https://doi.org/10.1063/1.4975435.

28. Okamura Y, Hinata N, Hoshiba T, Nakatsuji T, Ikeo N, Furukawa J, Harada K, Nakano Y, Fukumoto T, Mukai T, Fujisawa M. Development of bioabsorbable zinc–magnesium alloy wire and validation of its application to urinary tract surgeries. World J Urol. 2021;39:201–8. https://doi.org/10.1007/s00345-020-03138-7.

29. Kustra P, Wróbel M, Byrska-Wójcik D, Paćko M, Płonka B, Wróbel M, Sulej-Chojnacka J, Milenin A. Manufacture technology, mechanical and biocorrosion properties of the Zn and ZnMg0.008 alloy wires designed for biodegradable surgical threads. J Manuf Process. 2021;67:513–20. https://doi.org/10.1016/j.jmapro.2021.05.024.

30. Seitz J-M, Utermöhlen D, Wulf E, Klose C, Bach F-W. The manufacture of resorbable suture material from magnesium—drawing and stranding of thin wires. Adv Eng Mater. 2011;13:1087–95. https://doi.org/10.1002/adem.201100152.

31. Milenin A, Kustra P, Byrska-Wójcik D, Grydin O, Schaper M, Mentlein T, Gerstein G, Nürnberger F. Analysis of microstructure and damage evolution in ultra-thin wires of the magnesium alloy MgCa0.8 at multipass drawing. JOM. 2016. https://doi.org/10.1007/s11837-016-2127-3.

32. Liu C, Zhu X, Zhou H. Phase diagrams for magnesium alloy. Central South University Press; 2006. p. 63.

33. Biba N, Maximov A, Stebunov S, Vlasov A (2012) The model for simulation of thermally, mechanically and physically coupled problems of metal forming. In: Kusiak DSJ, Majta J (Eds) Proceedings of 14th International Conference on Metal Forming, Kraków, pp 1363–1366

34. Williamson GK, Hall WH. X-ray line broadening from filed aluminium and wolfram. Acta Metall. 1953;1:22–31. https://doi.org/10.1016/0001-6160(53)90006-6.

35. Shlomchack GG, Mamuzic I, Vodopivec F. Rheological similarity of metals and alloys. J Mater Process Tech. 1994;40:315–25. https://doi.org/10.1016/0924-0136(94)90458-8.

36. Slomchack GD, Milenin AA, Mamuzić I, Vodopivec F. A mathematical model of the formation of the plastic deformation zone in the rolling of rheologically complex metals and alloys. J Mater Process Technol. 1996;58:184–8. https://doi.org/10.1016/0924-0136(95)02099-3.

37. Häussermann U, Simak SI. Origin of the c/a variation in hexagonal close-packed divalent metals. Phys Rev B. 2001;64: 245114. https://doi.org/10.1103/PhysRevB.64.245114.